

Research  
Smart Grid and Energy Internet—Article

## Micro-Cantilever Electric Field Sensor Driven by Electrostatic Force

Zhifei Han<sup>a</sup>, Jun Hu<sup>a</sup>, Licheng Li<sup>b</sup>, Jinliang He<sup>a,\*</sup>

<sup>a</sup>State Key Lab of Power Systems, Department of Electrical Engineering, Tsinghua University, Beijing 100084, China

<sup>b</sup>China Southern Power Grid, Guangzhou 510623, China



### ARTICLE INFO

#### Article history:

Received 13 October 2021

Revised 22 May 2022

Accepted 20 June 2022

Available online 6 August 2022 xxxx

#### Keywords:

Microsensors

Electric sensing devices

Microfabrication

Piezoresistive devices

### ABSTRACT

With the development of smart grids and the energy internet, large-scale monitoring of voltage and electric field data is required in all aspects of power systems, which requires the arrangement of various advanced sensors. Measurement of the electric field can replace traditional voltage transformers to realize the non-contact measurement of voltage, which reduces the insulation cost and the difficulty of operation and maintenance. Electric field measurement can also be applied in various other areas, such as equipment fault diagnosis, lightning warning, and electromagnetic environment measurement. Traditional electric field measurement devices, such as field mills, are bulky and costly, so they cannot be arranged flexibly on a large scale. In this paper, we present an electrostatically actuated micro-electric field sensor (E-sensor) with a piezoresistive sensing structure. The presented E-sensor is fabricated into a four-cantilever structure using microfabrication technology. The cantilevers are displaced under the drive of the electrostatic force, and the generated strain is transformed into measurable signals through piezoresistive materials. The presented E-sensor has the advantages of small size, low cost, low power consumption, and easy mass production. Moreover, the E-sensor has a high signal-to-noise ratio, high resolution, and wide measuring range. The experimental results show that the E-sensor has a linear electric field measurement range from 1.1 to 1100.0  $\text{kV}\cdot\text{m}^{-1}$  with an alternating current (AC) resolution of up to  $112 \text{ V}\cdot\text{m}^{-1}\cdot\text{Hz}^{-1/2}$  and a cut-off frequency of 496 Hz, making it suitable for most applications in smart grids and the energy internet.

© 2022 THE AUTHORS. Published by Elsevier LTD on behalf of Chinese Academy of Engineering and Higher Education Press Limited Company. This is an open access article under the CC BY-NC-ND license (<http://creativecommons.org/licenses/by-nc-nd/4.0/>).

## 1. Introduction

Large-scale information monitoring is one of the foundations for the realization of smart grids and the energy internet [1–3]. Through the large-scale collection of voltage and current data, a control strategy for power systems can be optimized, and status monitoring and fault diagnosis of power systems and equipment can be realized [4]. High voltage is traditionally measured by a voltage transformer, which is bulky and has poor performance. Moreover, the need for insulation increases the cost of measurement and the difficulty of operation and maintenance. Given the need for an increasing number of sensing nodes, such large-volume and high-cost voltage-measuring equipment can no longer meet the demand. According to the Gauss–Legendre algorithm, voltage can be reversed by measuring the electric field at several points [5,6]. Therefore, with the use of an electric field sensor (E-

sensor), non-contact voltage measurement can be realized, which can reduce the cost of measurement and increase the quantity of sensing nodes [7,8]. In addition to voltage measurement, E-sensors can be used for the fault monitoring of electrical equipment [9–11]. It is difficult to implement status monitoring and fault diagnosis of electrical equipment online. When insulation failure or partial discharge occurs in electrical equipment, the internal electric field of the equipment will change. By arranging micro-E-sensors and extracting fingerprint characteristics of the electric field signal, such faults can be monitored and diagnosed online.

E-sensors have important applications in fields other than power systems as well, as shown in Fig. 1 [12]. Wearable E-sensors can be used for near-electricity warnings for electric workers [13]. E-sensors can also be used to monitor the electric field of the atmospheric, in order to realize lightning warning, weather forecasting, and the selection of space launch windows [14–17]. Furthermore, measurement of the electrostatic field can be used in industrial production as a means of safety monitoring, especially in the petrochemical industry. In addition, E-sensors can be used

\* Corresponding author.

E-mail address: [hejl@tsinghua.edu.cn](mailto:hejl@tsinghua.edu.cn) (J. He).

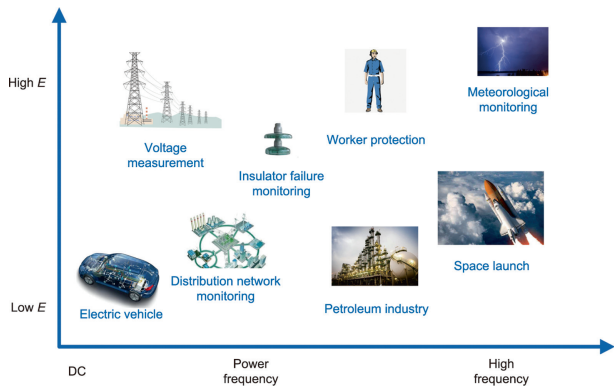


Fig. 1. Applications of micro-E-sensors.  $E$ : electric field.

for cabin monitoring in advanced electric vehicles and aircraft [18]. Application in such areas requires E-sensors to have high resolution, a wide measurable range, and low power consumption, in addition to a small size and low cost.

At present, electric field measurement presents numerous difficulties. For one thing, large and high-permittivity measuring devices will cause electric field distortion. For another, a complex electromagnetic environment often results in high coupling interference. In a power system, the amplitude of electric field measurement can reach the order of megavolts per meter, and the measurement frequency varies from direct current (DC) to kilohertz. At the same time, in order to meet the needs of most application scenarios in a power grid, the resolution of electric field measurement must be within  $200 \text{ V}\cdot\text{m}^{-1}$ . Field mills are traditionally used in the measurement of electric fields. However, due to the large size and low accuracy, this approach can no longer meet current needs. Microsensors are small advanced sensors with a low cost and high performance that can easily be mass produced using microfabrication technology. The principles behind micro-E-sensors include the electro-optical effect, charge induction, and the piezoelectric effect. The measurement of optical E-sensors is based on the change in the refractive index of electro-optic crystals under electric fields [19–23]. Optical E-sensors have a high resolution and wide frequency bandwidth and are currently used in applications such as bus voltage measurement in substations. Although such E-sensors are small, they need to be connected to expensive and bulky light sources and receivers through optical fibers, which cannot be arranged flexibly in equipment or on a large scale.

Electric fields can also be measured using the induced charges of a conductor in an electric field [24–27]. Micro-electro-mechanical system (MEMS) E-sensors based on charge induction are composed of a vibrating shield electrode, a fixed electrode for inducing charge, and back-end circuits. Such sensors have the

advantages of small size and low cost. However, they often introduce high noise interference, and it is difficult to improve their frequency response and resolution, due to the limitations of their sensing area. Micro-E-sensors based on the piezoelectric effect measure electric fields by sensing the deformation of piezoelectric materials under an electric field [28–31]. Such E-sensors are small and can be easily integrated. Nevertheless, the fabrication technology for piezoelectric materials and issues with the sensor performance—such as resolution and the signal-to-noise ratio—limit the application of such sensors.

In this paper, we present an electrostatically actuated micro-E-sensor with a piezoresistive sensing structure. The sensor is fabricated into a four-cantilever structure with grounded metal films arranged at the ends of the cantilevers. Driven by electrostatic force, the cantilevers bend up in an electric field. The strain generated by the bending of the cantilever causes a change in the resistance of the piezoresistive materials at the roots of the cantilevers. The electric field is measured according to the output signal of a Wheatstone bridge circuit with piezoresistive materials arranged on its arms. Compared with optical E-sensors, the presented E-sensor has a small size of  $8 \text{ mm} \times 8 \text{ mm}$  and can be mass produced at a low cost using silicon-based microfabrication technology. Compared with MEMS E-sensors, the presented E-sensor does not require additional shielded electrode drive sources. In addition, since the response frequency of the E-sensor is twice the frequency of the electric field, the coupling interference of the E-sensor can be effectively reduced. Moreover, because the harmonics in the power grid are mostly odd harmonics, the output signal at a double frequency makes the sensor more suitable for power systems. The experimental results show that the cut-off frequency of the E-sensor is as high as 496 Hz, and the measurable electric field ranges from 1.1 to  $1100.0 \text{ kV}\cdot\text{m}^{-1}$  with an alternating current (AC) resolution of  $112 \text{ V}\cdot\text{m}^{-1}\cdot\text{Hz}^{-1/2}$ . The performance of the presented E-sensor meets most of the application requirements for smart grids and the energy internet.

## 2. Working principle and structural design

When a metal film is placed in an electric field, the free charge carriers will redistribute, resulting in opposite charges at the surface of the metal film, as shown in Fig. 2(a). This polarization compensates for the electric field inside the metal. In an external electric field, these generated charges are subject to an outward electrostatic force, while the resultant force on the metal film remains at zero. If the lower surface of the metal film is grounded, the charges generated on the lower surface are transferred away, and the metal film is subject to an upward electrostatic force. When a metal film is prepared on the free end of a silicon cantilever, the cantilever will bend up under the drive of the metal film, as shown in Fig. 2(b). The electrostatic force ( $F_{\text{es}}$ ) on the metal film can be calculated as follows:

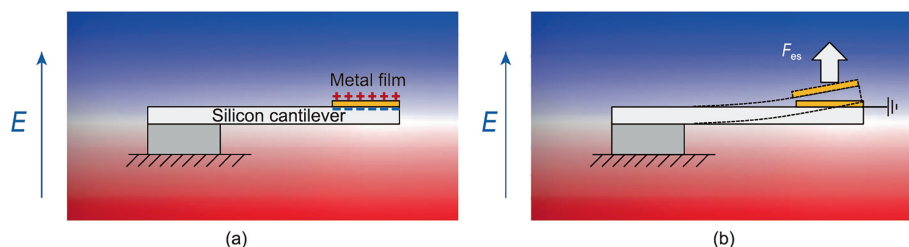


Fig. 2. Response of a silicon cantilever with metal film in an electric field. (a) Induced charges of the metal film; (b) force of the grounded metal film and displacement of the silicon cantilever.  $F_{\text{es}}$ : electrostatic force.

$$F_{es} = \frac{1}{2} \epsilon A E^2 \tag{1}$$

where  $A$  is the area of the metal film,  $E$  is the electric field along the normal direction of the film, and  $\epsilon$  is the dielectric constant of air.

The structure of the presented E-sensor is shown in Fig. 3. The sensor is designed as a four-cantilever structure, where the four cantilevers are symmetrically distributed. One end of each cantilever is fixed in the center of the silicon substrate column, while the other end of the cantilever can vibrate freely. A grounded metal film is prepared on the free end of each cantilever. Under the action of an electric field, the four cantilevers bend up with the same amplitudes, as shown in Fig. 3(a), generating stress inside the silicon cantilevers. At the fixed end of the cantilevers, four zigzag piezoresistive areas are prepared using ion doping. The piezoresistive areas are connected by metal electrodes to form a Wheatstone bridge circuit, as shown in Fig. 3(b).

When the strain of the four silicon cantilevers changes, the energy band of the doped silicon also changes, moving the energy of the energy valley. The stress of the doped silicon satisfies the following:

$$\sigma_l = \sigma_t / \nu \tag{2}$$

where  $\sigma_l$  is the stress along the length of the cantilever,  $\sigma_t$  is the stress perpendicular to the length of the cantilever, and  $\nu$  is the Poisson ratio of the doped silicon.

Under the silicon strain, the resistance of the four piezoresistive areas changes. Among the four piezoresistive areas,  $R_1$  and  $R_3$  are designed as a zigzag shape, which couples the strain along the length of the cantilever.  $R_2$  and  $R_4$  are designed as a straight strip shape, which couples the strain along the width of the cantilever. Thus, the resistance changes of the adjacent piezoresistive areas are reversed. The initial resistance values of the piezoresistive areas are designed to be the same to reduce zero drift. If we set the initial resistance of the four piezoresistive areas as  $R_0$  and mark the resistivity changes in  $R_1$  and  $R_3$  as  $\Delta R_a$  and the resistivity changes in  $R_2$  and  $R_4$  as  $\Delta R_b$ , then:

$$\begin{cases} \frac{\Delta R_a}{R_0} = P(N, T) \sigma_l (\pi_l + \nu \pi_t) \\ \frac{\Delta R_b}{R_0} = P(N, T) \sigma_t (\nu \pi_l + \pi_t) \end{cases} \tag{3}$$

where  $\pi_l$  and  $\pi_t$  are the piezoresistive coefficients in the longitudinal and transverse directions, respectively. In the designed E-sensor, the values of  $\pi_l$  and  $\pi_t$  are +71.3 and -66.7, respectively.  $P(N, T)$  is the coefficient that depends on the semiconductor doping density  $N$  and the temperature  $T$ .

When applying a constant voltage source  $U_s$  at the input ports  $U_s(+)$  and  $U_s(-)$  of the Wheatstone bridge, according to Kirchhoff's

laws, the output of the Wheatstone bridge  $U_o$  can be calculated as follows:

$$U_o = \frac{P(N, T) \sigma_l (\pi_l - \pi_t) (1 - \nu)}{2 + P(N, T) \sigma_l (\pi_l + \pi_t) (1 + \nu)} U_s \tag{4}$$

According to Eq. (4), under fixed doping conditions, the piezoresistive areas where the strain is the largest should be selected to increase the response of the E-sensor.

To verify the working principle of the presented E-sensor, we use the finite-element method (FEM) via Comsol Multiphysics to simulate the E-sensor response under different parameters and electric fields. To simplify the model, the surrounding fixed area of the E-sensor is omitted, while the fixed silicon column and four cantilevers are retained. The simulation uses the physics of electrostatics and solid mechanics and the multiphysics of electromechanical force. We set the cantilever to free boundary conditions. The boundary conditions of other areas are fixed. Fig. 4 shows the response of the E-sensor when an electric field of  $1 \text{ MV}\cdot\text{m}^{-1}$  is applied along the  $z$ -axis.

Figs. 4(a) and (b) show the distribution of the cantilever displacement. Under the electrostatic force, the metal film at the end of the cantilever drives the cantilever to bend upward. The four cantilevers have the same displacement. It is worth noting that the force on the cantilever is always upward, regardless of whether the direction of the electric field is along the positive or negative  $z$ -axis. Figs. 4(c) and (d) shows the distribution of the XX strain component on the cantilever. The YY strain component is symmetrical with the XX component. As shown in the figure, the largest strain component on the cantilever is located at the root of the cantilever. In order to maximize the sensor response, the ion-doped area is chosen to be close to the fixed area on the cantilever.

According to simulations, the maximum strain of the E-sensor increases linearly with the electric field. When the electric field is applied in the reverse direction along the  $z$ -axis, the sensor response is the same as the electric field is applied along the  $z$ -axis. In addition, the response of the E-sensor is related to the length and thickness of the cantilever. Simulations can provide a theoretical reference for designing the optimal parameters and layout of the E-sensor. Increasing the maximum strain of the cantilever under the same electric field can increase the output of the Wheatstone bridge, thereby increasing the resolution of the E-sensor. The relationship between the maximum strain tensor XX (eXX) on the cantilever and the length and thickness of the cantilever is shown in Fig. 5.

According to the principle of leverage, under the same electrostatic force, increasing the length of the cantilever increases the torque. Therefore, under the same electric field, the longer the cantilever is, the greater the maximum strain on the cantilever will be,

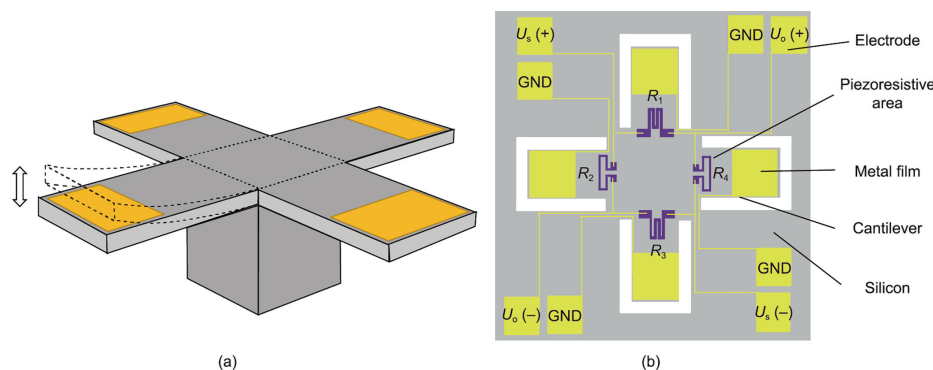


**Fig. 3.** Structure of the E-sensor. (a) Diagram of the E-sensor structure; (b) overhead view of the E-sensor structure and circuit. GND: ground;  $R_1$ – $R_4$ : piezoresistive areas;  $U_s$ : constant voltage source;  $U_o$ : output voltage.

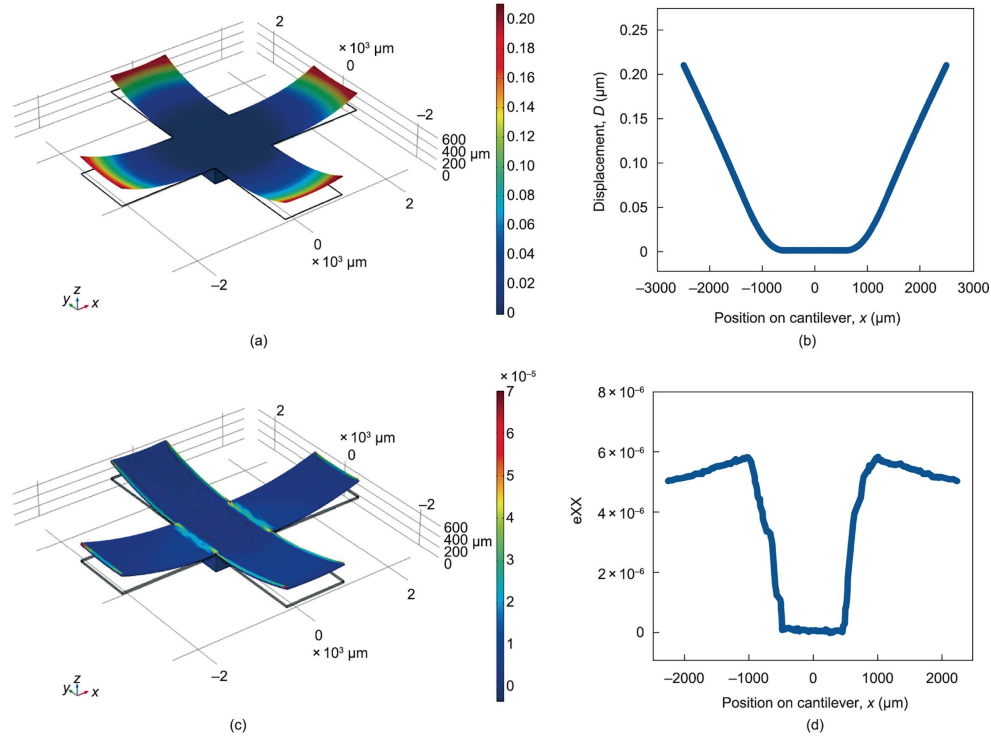


**Fig. 4.** Simulated response of the E-sensor. (a) Distribution of the displacement; (b) displacement curve of the cantilever; (c) distribution of the strain tensor XX ( $e_{XX}$ ); (d) cantilever curve for the strain tensor XX.

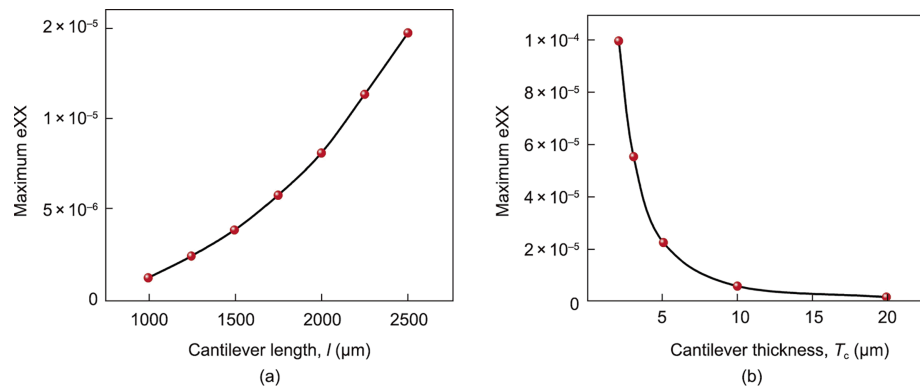


**Fig. 5.** Relationship between the maximum strain tensor XX on the cantilever and the length and thickness of the cantilever. (a) Maximum strain tensor XX under different cantilever lengths  $l$ ; (b) maximum strain tensor XX under different cantilever thicknesses  $T_c$ .

as shown in Fig. 5(a). Within a reasonable range, increasing the cantilever length improves the response of the E-sensor. However, an excessive cantilever length both reduces the mechanical strength of the cantilever and makes it more difficult to prepare the device. Moreover, as the length of the cantilever increases, the resonant frequency of the cantilever drops, causing the cut-off frequency of the E-sensor to decrease. Considering various factors such as device fabrication, lifetime, and device performance, the length of the fabricated E-sensor cantilever was selected to be within the range of 1250–2250  $\mu\text{m}$ .

Similarly, reducing the thickness of the cantilever increases the maximum strain on the cantilever, thereby increasing the E-sensor response, as shown in Fig. 5(b). However, a cantilever that is too thin will affect the fabrication difficulty and mechanical strength of the E-sensor. Thus, the cantilever thickness of our E-sensor was chosen to be 5 and 10  $\mu\text{m}$ .

Changing the metal film area affects the sensor response. According to Eq. (1), increasing the metal film area  $A$  increases the electrostatic force, thus increasing the sensor response. Therefore, the area of the metal film should be as large as possible. However, when the length of the metal film increases past a certain value, the increase in the sensor response becomes insignificant. Moreover, when the metal is close to the root of the cantilever, it may affect the fabrication of the piezoresistive material. Therefore, the metal film was fabricated at the end of the cantilever, and a length of 800  $\mu\text{m}$  was chosen. Section 4 shows a performance comparison of E-sensors with different parameters.

### 3. Device fabrication

Based on the theoretical analysis and simulation results of the designed E-sensor structure, the presented E-sensor was fabricated

using silicon-based microfabrication technology. The fabrication process was based on 10 cm diameter silicon-on-insulator (SOI) wafers with a device layer thickness of 5 and 10 μm and a box thickness of 1 μm. The crystal orientation of the device layer was selected to be <100> and the resistivity of the device silicon was 6–8 Ω·cm. About 90 E-sensors can be produced on one 10 cm diameter wafer.

A schematic illustration of the E-sensor fabrication process is provided in Fig. 6. The wafer is patterned and fabricated through a combination of photolithography technology and other microfabrication technologies. The six photolithography masks used in the fabrication process are shown in Fig. 7(a). After the SOI wafer is cleaned with a mixture of hot concentrated sulfuric acid and hydrogen peroxide, the piezoresistive area is patterned onto the device layer. In order to ion dope the piezoresistive area, the wafer is heated in an oxygen atmosphere to form a 20 nm silicon oxide layer on the surface. The oxide layer acts as a shielding layer for the ion doping. Next, boron ions are doped onto the device layer with a concentration of  $5 \times 10^{18} \text{ cm}^{-3}$ , forming a PN junction with a depth of 1.5 μm. The piezoresistive areas are created within the designed shape using photolithography, and ohmic contact areas are provided to ensure good ohmic contact between the piezoresistive areas and the electrodes. The wafer is annealed at 1000 °C for 30 min in a nitrogen atmosphere to activate the doped areas. After the piezoresistive areas are fabricated, a silicon oxide insulating layer with a thickness of 400 nm is grown on the surface of the wafer in an oxygen atmosphere. The insulating layer is then patterned using inductively coupled plasma (ICP) etching technology to release the silicon oxide in the ohmic contact area and the cantilever area. Finally, a metal layer composed of a chromium (Cr) layer and a gold (Au) layer is prepared on the surface of the device layer by means of magnetron sputtering. The metal is patterned into a Wheatstone bridge shape using photolithography and wet etching. In this way, the processing of structure on the device layer surface is completed.

Processing in the depth direction of the wafer is then performed. First, the device layer is patterned using ICP etching to form the shape of the cantilevers. Then, the handle layer under the cantilever structure is etched away. Finally, the box layer is etched away to release the four cantilevers. During the cantilever release, the temperature and time of the processing must be accurately controlled to ensure that the cantilevers have the same initial state. The fabricated wafer before dicing is shown in Fig. 7(b). The microstructure of the sensor chip is shown in Fig. 7(c).

Finally, the wafer is diced into  $8 \text{ mm} \times 8 \text{ mm}$  chips using laser cutting, as shown in Fig. 7(d). The metal electrodes on the E-sensor

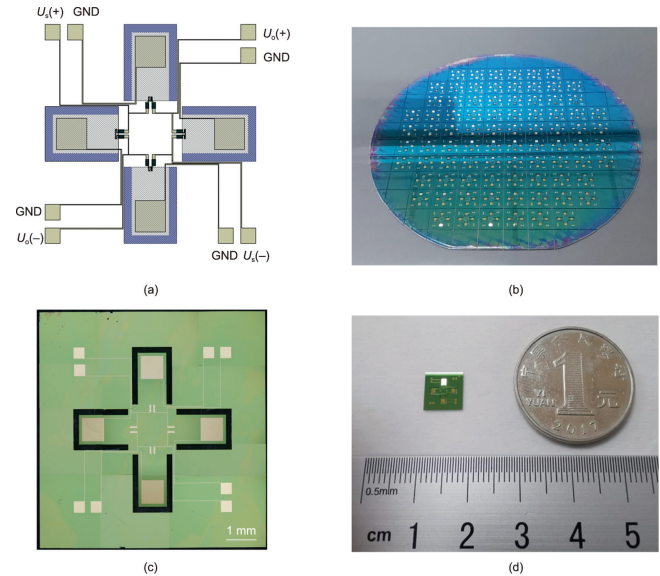


Fig. 7. The fabricated micro-E-sensor. (a) Masks for photolithography; (b) overall view of the 10 cm diameter wafer before dicing; (c) microscopic image of the E-sensor structure; (d) diagram showing the E-sensor size.

are welded to the printed circuit board (PCB) with gold wire. As discussed in Section 4, the PCB was used in an electric field test station to further test the E-sensor performance.

#### 4. Device performance

An electric field test station was built for the performance testing of the E-sensors, as shown in Fig. 8(a). The test station can generate electric fields with different field strengths, frequencies, and waveforms. In the test station, an electric field is generated by applying a voltage to a pair of circular metal electrodes. The ratio of the electrode diameter to the distance should be high enough to ensure a uniform electric field between the electrodes. A column for fixing the PCB board is arranged beside the two electrodes. The PCB board is designed as a “T” shape, as shown in Fig. 8(b). The E-sensor is placed on one end of the PCB, and the other end of the PCB is fixed by screws. The input voltage signal is generated by a generator (DG1022, Rigol Technology Inc., China) and amplified by a high-voltage amplifier (TREK MODEL 10/10B-HS, Trek Inc., USA)

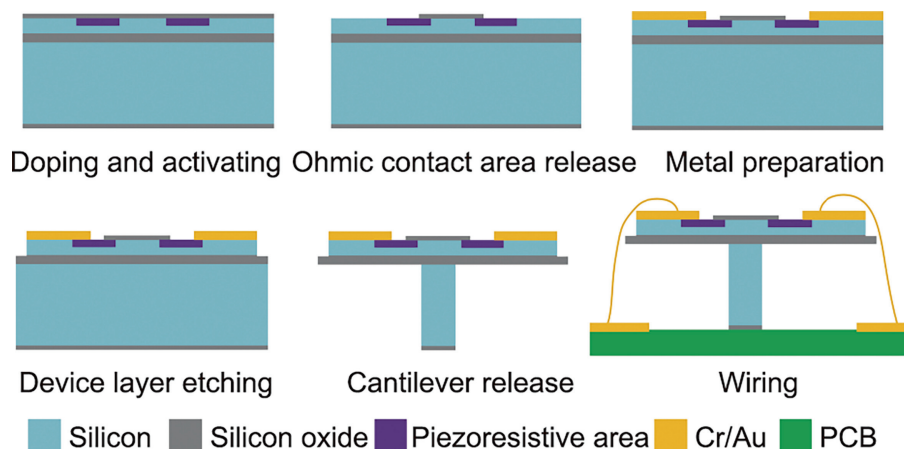
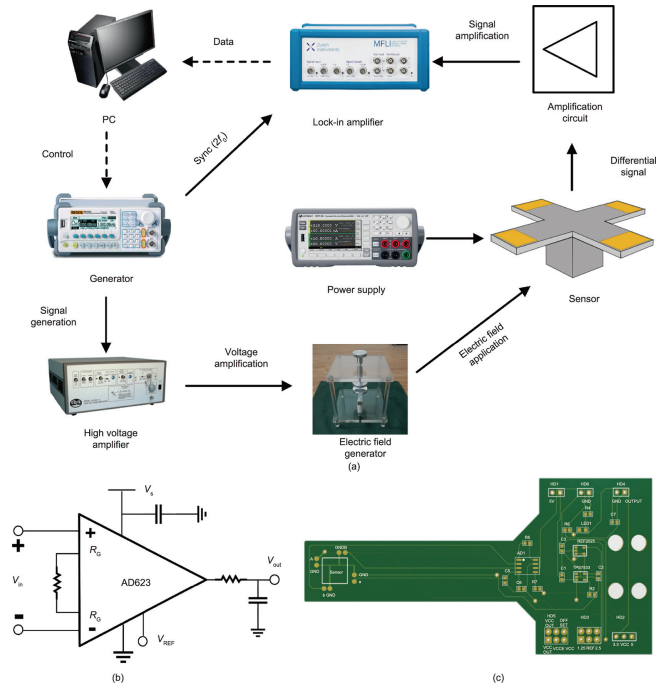


Fig. 6. Schematic illustration of the E-sensor fabrication. PCB: printed circuit board.



**Fig. 8.** Electric field measurement setup. (a) Schematic of the electric field measurement setup; (b) schematic of the PCB; (c) back-end differential amplification circuit. PC: personal computer; sync: synchronization signal;  $f_0$ : frequency of generator signal;  $R_G$ : external gain setting resistor,  $V_{in}$ : input signal,  $V_{out}$ : output signal,  $V_{REF}$ : output reference signal,  $V_S$ : positive supply terminal.

with a fixed gain of 1000. The output signal of the sensor is differentially amplified by the back-end circuit based on AD623, as shown in Fig. 8(c). The back-end circuit is arranged on the PCB. The amplified signal is used for frequency selection through a lock-in amplifier (MFLI, Zurich Instruments, Switzerland), based on a generator signal frequency twice as high as the synchronization signal frequency. In addition, a high-precision voltage source (B2912A, Keysight Technology Inc., USA) is used to provide a 6 V input signal to the Wheatstone bridge on the sensor chip. Based on a LabVIEW program, the output signal of the generator and the output of the lock-in amplifier are controlled and collected through a personal computer (PC).

Based on the electric test station, we tested the prepared E-sensors with different parameters under electric fields with different amplitudes and frequencies. The tests were carried out under stable environmental conditions with the air pressure maintained at 101 kPa, the temperature at  $(25 \pm 1)^\circ\text{C}$ , and the humidity at  $50 \pm 10\%$ . For electric field measurement, important parameters include the dynamic range, linearity, cut-off frequency, and resolution. The fabricated E-sensors were divided into four groups, marked as S1, S2, S3, and S4. Each group consisted of 10 sensor chips. The cantilever lengths of the E-sensors were 1250, 1750, and 2250  $\mu\text{m}$ , respectively. The cantilever thickness of the E-sensors was set to 5 and 10  $\mu\text{m}$ . Table 1 displays the performance of E-sensors with different parameters.

**Table 1**  
Results of electric field measurement for E-sensors with different parameters.

Sensor group	S1	S2	S3	S4
Cantilever length ( $\mu\text{m}$ )	1250	1750	2250	1750
Cantilever thickness ( $\mu\text{m}$ )	10	10	10	5
AC resolution ( $\text{V}\cdot\text{m}^{-1}\cdot\text{Hz}^{-1/2}$ )	301	253	236	112
Dynamic range ( $\text{V}\cdot\text{m}^{-1}$ )	$2.1 \times 10^3\text{--}1.1 \times 10^6$	$1.9\text{--}813.0 \times 10^3$	$1.6\text{--}749.0 \times 10^3$	$1.1\text{--}279.0 \times 10^3$
Cut-off frequency (Hz)	496	474	441	296

The four groups of E-sensors were tested under different electric field strengths at 50 Hz. The output voltages of the E-sensors are shown in Fig. 9(a). At a fixed frequency, the amplitude response of the E-sensors exhibits high linearity. The output voltage curve is linearly fitted, and the coefficient of determination ( $r^2$ ) values of Sensors S1–S4 are 0.998, 0.998, 0.998, and 0.996, respectively. In line with the theoretical analysis and simulation results, increasing the length or reducing the thickness of the cantilever increased the response of the E-sensor. Combining the response curves of the E-sensors with the actual sources of noise and interference, the AC resolution of the E-sensors was calculated, as shown in line 4 of Table 1. When the electric field strength is too large or too small, the response of the E-sensor no longer exhibits linearity. When the electric field is high, the response curve of the sensor bends downward, because the response of the E-sensors is too large, and the working mode is changed. Under a low electric field, the influence of noise increases significantly. In addition, the interference of the environment and temperature causes the sensor to exhibit zero drift, which is manifested as the intercept of the output voltage curve. Taking the linearity of the response curve  $r^2 > 0.99$  as the limiting condition, the linear measurable electric field range (i.e., the dynamic range) of the E-sensors can be obtained, as shown in line 5 of Table 1.

Fig. 9(b) shows the frequency response curves of E-sensors with different parameters. Below the resonant frequency of the device, the E-sensor response curves are relatively flat. Taking a 3 dB change as the range, the cut-off frequencies of Sensors S1–S4 are 496, 474, 441, and 296 Hz, respectively. The difference in the resonant frequencies of the sensors is caused by the difference in the size parameters of the sensor structure. Consistent with the theoretical analysis, reducing the length or increasing the thickness of the cantilever increases the resonance frequency of the mechanical structure, thereby increasing the cut-off frequency of the E-sensor. However, the increase in cut-off frequency is accompanied by a decrease in sensor response. Therefore, the size parameters of the E-sensor must be designed according to actual application scenarios. Above the resonance frequency, the response of the E-sensor decreases rapidly. When the frequency is too low, the response of the E-sensor gradually decreases as well. It is worth noting that the sensor also responds to the DC electric field, but the output voltage will gradually decrease over time.

Fig. 9(c) shows the frequency response curve of Sensor S2 under different electric field strengths. As the electric field strength increases, the cut-off frequency of the E-sensor remains basically unchanged. When the field strength is low, the signal-to-noise ratio of the sensor is greatly affected by noise. At a high field strength, the signal-to-noise ratio of the E-sensor output signal is high, but it is limited by the maximum output voltage of the lock-in amplifier.

The experimental results show that the E-sensor has a high performance and high consistency under different electric fields. The AC resolution of the E-sensor can reach  $112 \text{ V}\cdot\text{m}^{-1}\cdot\text{Hz}^{-1/2}$ , the linear dynamic range can reach  $1.1\text{--}1100 \text{ kV}\cdot\text{m}^{-1}$ , and the cut-off frequency is 496 Hz. Under normal operating conditions, the power consumption of the sensor is on the order of microwatts. In addition, the double frequency response enables the output signal of

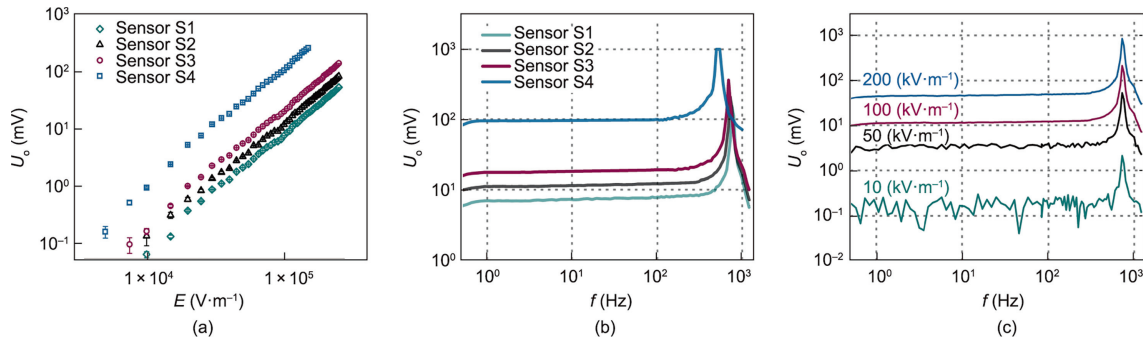


**Fig. 9.** Response curves of E-sensors under electric fields. (a) Experimental static output  $U_o$  versus electric field  $E$  of E-sensors with different parameters; (b) frequency ( $f$ ) response curves of E-sensors with different parameters; (c) frequency response curves of Sensor S2 under different electric field strengths.

**Table 2**

Comparison of the characteristics of E-sensors based on different principles.

Principle	Amplitude range	Cut-off frequency	Resolution	Power consumption	Size	Cost	Signal-to-noise ratio	Temperature stability	Fabrication difficulty
Electro-optical effect	$< 1.00 \text{ MV}\cdot\text{m}^{-1}$	100 MHz	$500.0 \text{ V}\cdot\text{m}^{-1}$	Medium	Large	High	Low	Low	High
Piezoelectric effect	$< 1.57 \text{ MV}\cdot\text{m}^{-1}$	100 kHz	$12.7 \text{ V}\cdot\text{m}^{-1}$	Low	Small	Low	High	High	High
Charge induction	$< 100.00 \text{ kV}\cdot\text{m}^{-1}$	1 kHz	$20.0 \text{ V}\cdot\text{m}^{-1}$	Medium	Small	Low	High	High	Low
Electrostatic force (in this paper)	$1.10 \text{ V}\cdot\text{m}^{-1}$ – $1.10 \text{ MV}\cdot\text{m}^{-1}$	496 Hz	$112.0 \text{ V}\cdot\text{m}^{-1}$	Low	Small	Low	Low	High	Low

the E-sensor to be easily separated from the coupling signal, which greatly improves the signal-to-noise ratio. Table 2 compares the performance and characteristics of the presented E-sensor and E-sensors based on other principles. The presented E-sensor exhibits good performance in terms of measurement range, resolution, elimination of coupled noise, and power consumption, and can meet the needs of most electric field measurement scenarios. In the future, the cut-off frequency of the presented E-sensor needs to be further improved.

## 5. Conclusions

In this paper, we presented an electrostatically actuated E-sensor with a piezoresistive cantilever sensing structure. The presented E-sensor can be used for high-resolution electric field measurement in power systems and electrical equipment. Through theoretical calculation and a finite-element simulation method, the working principle of the E-sensor was verified, and the parameters of the E-sensor were optimized. We designed the fabrication process based on microfabrication technology and carried out sensor fabrication using 10 cm diameter SOI wafers. The experimental results showed that the presented E-sensor has high linearity and resolution. The AC resolution of the E-sensor can reach  $112 \text{ V}\cdot\text{m}^{-1}\cdot\text{Hz}^{-1/2}$ , the linear dynamic range can reach  $1.1$ – $1100.0 \text{ kV}\cdot\text{m}^{-1}$ , and the cut-off frequency is 496 Hz; thus, the sensor can meet the needs of most applications in power grids. The presented E-sensor also has the advantages of small size, low cost, easy mass production, and low power consumption. Moreover, the output signal of the E-sensor can be separated from the coupled noise by a double frequency lock using a lock-in amplifier, improving the signal-to-noise ratio of the output signal. The cut-off frequency of the presented E-sensor still requires further improvement in the future. In addition, by integrating micro-E-sensors with an energy-acquisition module, communication module, and data-processing module, the construction of high-performance sensor nodes can be realized. This high-performance electric field measurement system will play an important role in system detection and sensor network architecture in smart grids and the energy internet.

## Acknowledgments

This work was supported in part by the National Natural Science Foundation of China (51720105004, 51921005, and 52125703).

## Compliance with ethics guidelines

Zhifei Han, Jun Hu, Licheng Li, and Jinliang He declare that they have no conflict of interest or financial conflicts to disclose.

## References

- [1] Huang Q, Crow ML, Heydt GT, Zheng JP, Dale SJ. The future renewable electric energy delivery and management (FREEDM) system: the energy internet. *Proc IEEE* 2011;99(1):133–48.
- [2] Gubbi J, Buyya R, Marusic S, Palaniswami M. Internet of Things (IoT): a vision, architectural elements, and future directions. *Future Gener Comput Syst* 2013;29(7):1645–60.
- [3] Wu D, Zhou C. Fault-tolerant and scalable key management for smart grid. *IEEE Trans Smart Grid* 2011;2(2):375–81.
- [4] Chen K, Huang C, He J. Fault detection, classification and location for transmission lines and distribution systems: a review on the methods. *High Voltage* 2016;1(1):25–33.
- [5] Si D, Wang J, Wei G, Yan X. Method and experimental study of voltage measurement based on electric field integral with Gauss–Legendre algorithm. *IEEE Trans Instrum Meas* 2020;69(6):2771–8.
- [6] Zhang B, Hao Z, Bo Z. Development of relay protection for smart grid (1): new principle of fault distinction. *Electr Power Autom Equip* 2010;30(1):1–6. Chinese.
- [7] Yang P, Wen X, Chu Z, Ni X, Peng C. Non-intrusive DC voltage measurement based on resonant electric field microsensors. *J Micromech Microeng* 2021;31(6):064001.
- [8] Zhu J, Lei X, Su Z, Liu T, Liu K, Yu G, et al. Study of non-contact voltage detector of 1000 kV UHV AC based on MEMS electric field sensor. *MATEC Web Conf* 2018;160:02001.
- [9] Duan L, Hu J, Zhao G, Chen K, Wang SX, He J. Method of inter-turn fault detection for next-generation smart transformers based on deep learning algorithm. *High Voltage* 2019;4(4):282–91.
- [10] Chen W, Wang J, Wan F, Wang P. Review of optical fibre sensors for electrical equipment characteristic state parameters detection. *High Voltage* 2019;4(4):271–81.
- [11] Nitsch M, Camp M, Sabath F, terHaseborg JL, Garbe H. Susceptibility of some electronic equipment to HPEM threats. *IEEE Trans Electromagn Compat* 2004;46(3):380–9.
- [12] Han Z, Xue F, Hu J, He J. Micro electric-field sensors: principles and applications. *IEEE Ind Electron Mag* 2021;15(4):35–42.

- [13] Zeng S, Powers JR, Newbraugh BH. Effectiveness of a worker-worn electric-field sensor to detect power-line proximity and electrical-contact. *J Safety Res* 2010;41(3):229–39.
- [14] Yang P, Chen B, Wen X, Peng C, Xia S, Hao Y. A novel MEMS chip-based ground atmospheric electric field sensor. *J Electron Inf Technol* 2016;38(6):1536–40. Chinese.
- [15] Yang P, Chen B, Wen X, et al. A novel MEMS chip-based atmospheric electric field sensor for lightning hazard warning applications. *Proceedings of the 2015 IEEE Sensors*; 2015 Nov 1–4; Busan, Korea. Berlin: IEEE Xplore; 2015.
- [16] Mohammed R, Sabu S, Joby NE, et al. Electric field sensor for lightning early warning system. *Proceedings of the AGU 2017 Fall Meeting*; 2017 Dec 11–15; New Orleans, LA, USA, 2017.
- [17] Xu B, He H, Yang X, Bie Y, Lv Q. The study of meteorological effects and time variations of the fair weather atmospheric electric field near ground in YBJ, Tibet. *Acta Phys Sinica* 2012;61(17):175203. Chinese.
- [18] Kasaba Y, Hayakawa H, Ishisaka K, Okada T, Matsuoka A, Mukai T, et al. Evaluation of DC electric field measurement by the double probe system aboard the Geotail spacecraft. *Adv Space Res* 2006;37(3):604–9.
- [19] Tajima K, Kobayashi R, Kuwabara N, Tokuda M. Development of optical isotropic E-field sensor operating more than 10 GHz using Mach-Zehnder interferometers. *IEICE Trans Electron* 2002;85(4):961–8.
- [20] Zeng R, Chen W, He J, Zhu P. The development of integrated electro-optic sensor for intensive electric field measurement. *Proceedings of the 2007 IEEE International Symposium on Electromagnetic Compatibility*; 2007 Jul 9–13; Honolulu, HI, USA. Berlin: IEEE Xplore; 2007.
- [21] Zeng R, Wang B, Yu Z, Niu B, Hua Y, et al. Integrated optical E-field sensor based on balanced Mach-Zehnder interferometer. *Opt Eng* 2011;50(11):114404.
- [22] Zeng R, Yu J, Wang B, Niu B, Hua Y. Study of an integrated optical sensor with mono-shielding electrode for intense transient E-field measurement. *Measurement* 2014;50:356–62.
- [23] Wu Z, Lin Y, Han S, Yin X, Ding M, Guo L, et al. Simulation and analysis of micro-ring electric field sensor based on a lithium niobate-on-insulator. *Crystals* 2021;11(4):359.
- [24] Riehl PS, Scott KL, Muller RS, Howe RT, Yasaitis JA. Electrostatic charge and field sensors based on micromechanical resonators. *J Microelectromech Syst* 2003;12(5):577–89.
- [25] Peng C, Chen X, Ye C, Tao H, Cui G, Bai Q, et al. Design and testing of a micromechanical resonant electrostatic field sensor. *J Micromech Microeng* 2006;16(5):914–9.
- [26] Bahreyni B, Wijeweera G, Shafai C, Rajapakse A. Analysis and design of a micromachined electric-field sensor. *J Microelectromech Syst* 2008;17(1):31–6.
- [27] Ma Q, Huang K, Yu Z, Wang Z. A MEMS-based electric field sensor for measurement of high-voltage DC synthetic fields in air. *IEEE Sens J* 2017;17(23):7866–76.
- [28] Han Z, Xue F, Yang J, Hu J, He J. Micro piezoelectric-capacitive sensors for high-sensitivity measurement of space electric fields. *Proceedings of the 2019 IEEE Sensors*; 2019 Oct 27–30; Montreal QC, Canada. Berlin: IEEE Xplore; 2019.
- [29] Han Z, Xue F, Yang G, Yu Z, Hu J, He J. Micro-cantilever capacitive sensor for high-resolution measurement of electric fields. *IEEE Sens J* 2021;21(4):4317–24.
- [30] Xue F, Hu J, Guo Y, Han G, Ouyang Y, Wang SX, et al. Piezoelectric-piezoresistive coupling MEMS Sensors for measurement of electric fields of broad bandwidth and large dynamic range. *IEEE Trans Ind Electron* 2020;67(1):551–9.
- [31] Xue F, Hu J, Wang SX, He J. Electric field sensor based on piezoelectric bending effect for wide range measurement. *IEEE Trans Ind Electron* 2015;62(9):5730–7.